IEEE Robotics and Automation Letters (RA-L) paper, presented at ICRA 2026, Vienna, Austria. Cite as RA-L paper.

Estimation of Slip Ratio and Side Slip Angle of Wheeled Planetary Rovers Based on Trace Imprint

Nan Li, Junlong Guo, Liang Ding, *Senior Member*, *IEEE*, Chenghua Tian, Chuan Zhou, Haibo Gao

***Abstract*—This paper proposes a method to estimate the wheel slip ratio and side slip angle of wheeled rovers by processing images of wheel trace imprints. The proposed method extracts structural features from trace imprint images, such as the trace unit, trace contour, and angle between the centerline of the trace unit and contour. The relationships between the structural trace imprint features and the wheel slip ratio and side slip angle have been revealed after a study of the underlying mechanism of trace imprint formation, with consideration of the kinematics of the wheel lug and lug-soil interaction. These relationships are then used to estimate wheel slip ratio and side slip angle. Compared with the existing estimation methods, the proposed method can estimate longitudinal slippage and lateral drift simultaneously that typically occur in planetary rovers during traverse of cross slopes. The effectiveness of the proposed method has been demonstrated by experiments using a rover wheel test-bed under various conditions.**

***Index Terms*—Planetary rover, slip ratio, side slip angle, wheel trace imprint.**

I. Introduction

When traversing on soft and rough terrains on the moon or Mars, a planetary rover is prone to slipping longitudinally or laterally. The "Opportunity" rover became stuck in soft sand on Mars in 2005 due to excessive wheel slip [1-2]. It is necessary to monitor wheel slip states to avoid such hazardous situation. The wheel slip states are usually quantitatively depicted in slip ratio and side slip angle. These two parameters also play an important role in motion control and navigation [3]. For instance, they were taken as feedback variables in coordinated motion control of rover wheels to improve drive efficiency [4-7].

One of the most widespread techniques used to estimate rover slip ratio is based on Visual Odometry (VO). For example, slip ratio can be calculated with rover actual velocity getting from stereo imagery and theoretical velocities obtained from encoders [8]. Nevertheless, the VO-based approach is computationally expensive, which can negatively impact the mean rover drive speed, and replaced by optical flow method to obtain the actual velocity when working with TOF camera. To further improve estimation accuracy, multi-sensor fusion method was introduced. For instance, a longitudinal slip detection algorithm used an extended Kalman filter to integrate measurements from a GPS, an inertial measurement unit, and wheel encoders [9].

Different from the abovementioned works, slip ratio can also be estimated using a simplified model of motor current and wheel slip ratio [10]. However, this method required terrain-specific parameters to solve the simplified model and was undesirable for implementation. An approach using wheel-terrain interaction mechanics to estimate wheel slip ratio was proposed in 2009 [11].

The latest research started to detect slip ratio with machine learning methods. For example, a learning algorithm based on past experience was used to quantitatively predict slip ratio by terrain features [12]. Since learning requires a large amount of pre-training data, machine learning methods are poorly applicable to completely unknown planetary environments.

Three estimation approaches have been reported in the literature to estimate side slip angle: kinematics-based estimation, dynamics-based estimation, and wheel trace-based estimation. The kinematics-based methods did not need vehicle parameters or wheel-terrain conditions [13-14], but required acceleration measurement whose bias accumulated inevitably in the integration. The dynamics-based estimation method estimated side slip angle of ground vehicles, but cannot be applied to space rovers which typically works in much lower speeds [15]. The wheel trace-based estimation method used a robust Hough transform enhanced by fuzzy reasoning to estimate the inclination angle of the wheel trace with respect to the vehicle reference frame [16-17].

Few of the aforementioned methods can acquire both slip ratio and side slip angle simultaneously. This paper proposes a method to simultaneously estimate slip ratio and side slip angle using trace imprint images. Comparing to the state of the art, the slip ratio can be estimated with a higher accuracy [18], and the side slip angle can also be estimated with a higher accuracy under a wider range of experimental conditions [19]. However, this method is applicable only to sandy terrains.

The rest of the paper is organized as follows. Section II describes the formation mechanism of trace imprint with longitudinal slip. Section III extends the formation mechanism to trace imprint with coupled longitudinal slip and lateral slip.

Manuscript received: February 21, 2025; Revised: May 10, 2025; Accepted: June 10, 2025.

This paper was recommended for publication by Editor Lucia Pallottino upon evaluation of the Associate Editor and Reviewers' comments.

This study was supported in part by the National Natural Science Foundation of China (Grant No. 52275012/52005122); and the Independent Project of State Key Laboratory of Robotics and Systems (SKLRS202006B).

N. Li, J. Guo, L. Ding, and H. Gao are with the State Key Laboratory of Robotics and Systems, Harbin Institute of Technology, Harbin 150080, Heilongjiang, China (e-mail: lnlinanln@126.com, {junlongg, liangding, gaohaibo}@hit.edu.cn). C. Tian is with the Robot Division of Beijing Research Institute of Automation for Machinery Industry Co., Ltd., Beijing 100006, Beijing, China (tianchh@riamb.ac.cn). C. Zhou is with the Department of Minzu University of China, Beijing 100081, Beijing, China (e-mail: zhouchuan@tju.edu.cn).

All correspondence should be addressed to: J. Guo (junlongg@hit.edu.cn).

Digital Object Identifier (DOI): see top of this page.

In Section IV, the estimation models of wheel side slip and slip ratio are presented. A corresponding image process pipeline of trace imprint is established in Section V. Experimental results and discussions are presented in Section VI. Section VII summarizes this study.

II. Formation Mechanism of Wheel Trace Imprint with Longitudinal Slip

We intend to expound the formation mechanism of wheel trace imprint. To demonstrate the formulation mechanism in three dimensions, a simpler case without lateral slip was firstly studied in two dimensions.

A. Wheel Trace Imprint Description

A wheel trace imprint is the indentation of a wheel traversing sandy terrain. Most wheels in rovers are rigid with straight through-lugs, such as the wheels of the "Spirit" and "Opportunity". Figure 1 (a) shows the wheel imprint taken by the "Opportunity" rover on the Mars getting denser with the longitudinal slope gradient.

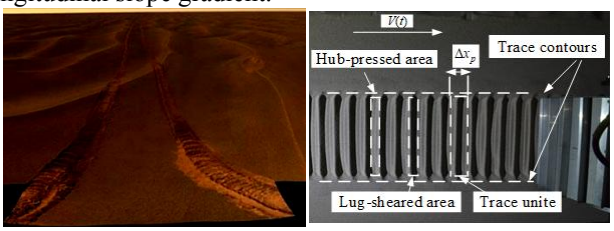

Fig. 1. (a) The trace left behind the "Opportunity" rover on the Mars, and (b) the trace imprint formation illustration and definition symbols.

A clearer and more intact wheel imprint pattern in longitudinal slip is shown in Fig. 1 (b). To explicitly describe trace imprint, several necessary symbols are annotated on it. The trace contours can be depicted to distinguish the wheel-terrain interaction and the non-interaction parts. The interaction area consists of a series of trace units, and each trace unit can be divided into two areas: the lug-sheared area dug by the lug and the hub-pressed area compactified by the wheel hub as shown in Fig. 2. The lug-sheared area and hub-pressed area occurring alternatively presents a staggered pattern of the trace imprint. The distance between two adjacent trace units is denoted as Δx_p.

Longitudinal slip ratio of a grouser-wheel is defined as:

$$s(t) = 1 - \frac{v(t)}{r_s \omega(t)} \tag{1}$$

where ω is angular velocity, r_s is shearing radius, v is wheel forward velocity, and t is time.

Several imprint patterns left by a wheel moving with various slip ratios are shown in Fig. 2. The distance Δx_p decreases with slip ratio, which means that the lug imprint of the trace become more condensed with a higher slip ratio.

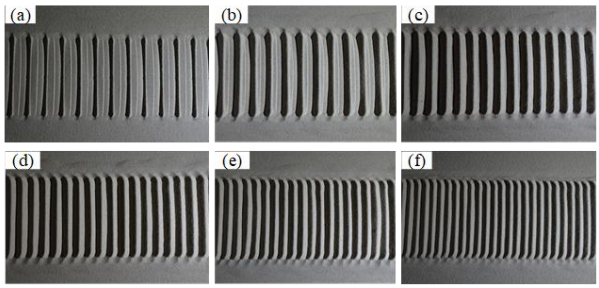

Fig. 2. The trace imprint with various slip ratios: (a) s=0; (b) s=0.1; (c) s=0.2; (d) s=0.3; (e) s=0.4; (f) s=0.5.

B. Wheel-Terrain Interaction and Lug Trajectory Analysis

A complete lug-terrain interaction process can be divided into three phases as shown in Fig. 3: initial phase, slippage phase, and departure phase. When the wheel moves forward without turning or lateral motion, the imprint of initial phase and slippage phase will be covered and mainly left the imprint formed in the departure phase.

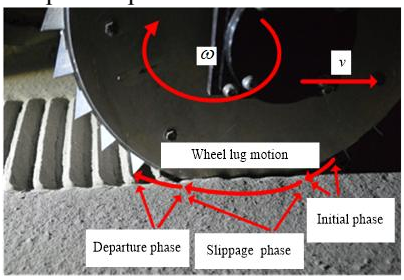

Fig. 3. The process of lug-terrain interaction without lateral slip.

To better clarify the trace formation, a schematic diagram of lug-terrain interaction process is portrayed in Fig. 4. A world coordinate frame is set on the terrain surface below the initial position of wheel center with X-axis aligning with the direction of $v(t)$ and Z-axis perpendicular to the terrain surface. The wheel sinks while the trace is formed. z_0 is the distance between the terrain surface and the bottom of wheel hubs and named as wheel sinkage.

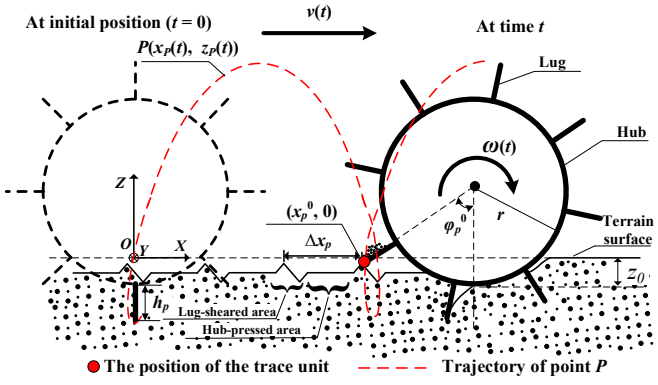

Fig. 4. Schematic of the process of lug-terrain interaction; $v(t)$ is wheel moving forward velocity; $\omega(t)$ is wheel angular velocity.

Any point P on the lug is in cycloidal motion during wheel rotation. It is the initial state that the wheel lug of point P is perpendicular to the horizon. The lug height is h. If the distance between P and the wheel hubs is $h_p(0 \le h_p \le h)$, the position of P at time t expressed in $(x_p(t), z_p(t))$ can be deduced with a generalized cycloid as:

IEEE Robotics and Automation Letters (RA-L) paper, presented at ICRA 2026, Vienna, Austria. Cite as RA-L paper.

$$\begin{cases} x_p(t) = \int_0^t v(\tau)\mathrm{d}\tau - (r+h_p)\sin\left[\int_0^t \omega(\tau)\mathrm{d}\tau\right] \\ z_p(t) = (r+h_p)\left\{1-\cos\left[\int_0^t \omega(\tau)\mathrm{d}\tau\right]\right\} - z_0 - h_p \end{cases} \quad (2)$$

The wheel velocity with slip can be given by

$$v(t) = [1-s(t)]r_s\omega(t) \quad (3)$$

Therefore, when the wheel slips, the trajectory of P is

$$\begin{cases} x_p(t) = \int_0^t [1-s(\tau)]r_s\omega(\tau)\mathrm{d}\tau - (r+h_p)\sin\left[\int_0^t \omega(\tau)\mathrm{d}\tau\right] \\ z_p(t) = (r+h_p)\left\{1-\cos\left[\int_0^t \omega(\tau)\mathrm{d}\tau\right]\right\} - z_0 - h_p \end{cases} \quad (4)$$

The wheel rotation angle is $\varphi(t) = \int_0^t \omega(\tau)\mathrm{d}\tau$; therefore,

$$\begin{cases} x_p(\varphi) = \int_0^{\varphi} r_s(\psi)[1-s(\psi)]\mathrm{d}\psi - (r+h_p)\sin\varphi \\ z_p(\varphi) = (r+h_p)(1-\cos\varphi) - z_0 - h_p \end{cases} \quad (5)$$

The lug trajectory is a general cycloid obtained by (5), as shown in Fig. 5. The trajectory is a long-amplitude cycloid.

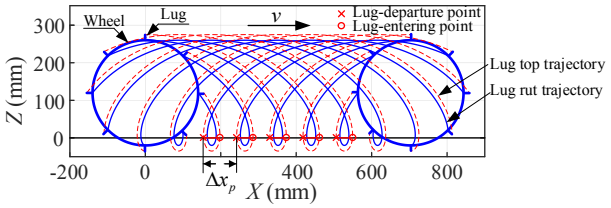

Fig. 5. The simulation of lugs' trajectories.

If $z_p \le 0$, wheel interacts with terrain. There are two boundary points that are the lug-entering and the lug-departure point. They are the junctions of the lug trajectory point and the X-axis. If the wheel moves without lateral slip, the lug imprint cannot form in the lug-entering point, but only in the lug-departure point. The position of lug-departure point in the trace unit is (x_p^0, 0); and its rotation angle is φ_p^0. According to (5) the position equation of the trace unit can be expressed by:

$$\begin{cases} x_p^0 = x(\varphi_p^0) = \int_0^{\varphi_p^0} r_s[1-s(\psi)]\mathrm{d}\psi - (r+h_p)\sin\varphi_p^0 \\ 0 = z(\varphi_p^0) = (r+h_p)(1-\cos\varphi_p^0) - z_0 - h_p \end{cases} \quad (6)$$

And the average shearing radius can be defined as [13]:

$$r_s = r + \lambda_s h \quad (7)$$

where h is the lug height and λ_s is the lug shearing coefficient.

And (6) can be simplified as:

$$\begin{cases} x_p^0 = x(\varphi_p^0) = r_s(1-\bar{s})\varphi_p^0 - (r+h_p)\sin\varphi_p^0 \\ \varphi_p^0 = \arccos\dfrac{r-z_0}{r+h_p} \end{cases} \quad (8)$$

The lug number is denoted as n. If the wheel rotates one revolution, n trace units will be formed on the terrain. The angle interval of the wheel rotation is $\Delta\varphi = 2\pi/n$ and the time interval $\Delta t_p = 2\pi/(n\bar{\omega})$. The distance that the wheel moves in one revolution is $x(\varphi_p^0+2\pi)$-$x(\varphi_p^0)$. Therefore, the width of trace unit is

$$\Delta x_p = \frac{x(\varphi_p^0+2\pi) - x(\varphi_p^0)}{n} \quad (9)$$

Combining (8) and (9) yields the width of the trace unit

$$\Delta x_p = \frac{2\pi(1-\bar{s})r_s}{n} \quad (10)$$

Figure 6 shows the trajectory of the lugs and hubs under various slip ratios. All wheels rotated 720° in the simulation. Comparing the trajectory under constant slip ratio of 0, 0.2, and 0.4 separately, there is a negative correlation between $\bar{s}$ and the wheel forward distance. Moreover, $\Delta x_{p1} > \Delta x_{p2} > \Delta x_{p3}$ indicating that Δx_p is in a negative relation with $\bar{s}$.

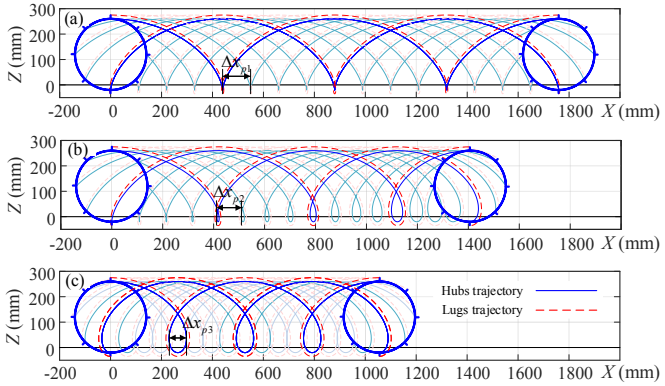

Fig. 6. The trajectory of lugs and hubs for various s, with (a) $s(\varphi) = 0$; (b) $s(\varphi) = 0.2$; (c) $s(\varphi) = 0.4$.

III. Formation Mechanism of Wheel Trace Imprint Coupling with Lateral and Longitudinal Slip

In Section II, the mechanism of trace imprint with longitudinal slip was discussed, which is a special motion state that the rover moves on non-lateral slope. However, when moving in rough and deformable terrain, the rover may slip laterally due to a force component along the wheel axis direction. In this section, the formation mechanism of the wheel trace imprint coupled with longitudinal and lateral slip will be analyzed in three-dimensional space.

A. Wheel Trace Imprint Formed Mechanism

When a rover moves on a lateral slope, its velocity can be decoupled as shown in Fig. 7. Set the coordinate origin O on the terrain surface under the wheel center; the Z-axis is along the gravity; the X-axis is along the direction of wheel velocity; the Y-axis is orthogonal to X-axis and Z-axis.

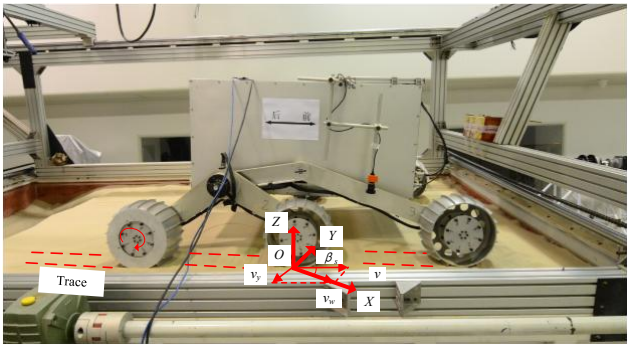

Fig. 7. Picture of a rover crossing lateral slopes with a constant angular velocity.

The v is rover linear velocity. Since the existence of lateral slope, there is a side slip velocity v_y along the lateral slope on the wheel. v_y is orthogonal to v. v_w is the resultant velocity of v and v_y. Side slip angle β_s between v_w and v can be expressed as:

IEEE Robotics and Automation Letters (RA-L) paper, presented at ICRA 2026, Vienna, Austria. Cite as RA-L paper.

$$\beta_s = \arccos\left(\frac{v(t)}{v_w(t)}\right) \tag{11}$$

The slip ratio for a wheel with side slip angle β_s can be deduced by substituting $v(t)$ into (1), as given in (12).

$$s(t) = 1 - \frac{v_w(t)\cos\beta_s}{r_s\omega(t)} \tag{12}$$

Wheel trace imprint coupling with longitudinal and lateral slip (Fig. 8 (a)) shows a different pattern from the trace imprint without lateral slip in Section II. Since the direction of wheel motion deviates from that of wheel heads, the trace imprint forms while separates, thus the trace imprint formed in the initial phase, slippage phase, and departure phase are maintained separately. A trace imprint unit can be divided into initial phase imprint, slippage phase imprint, and departure phase imprint, as shown in Fig. 8 (b).

To explicit describe the wheel trace imprint coupling with longitudinal and lateral slip, some new symbols relative to non-lateral slip are introduced, as annotated in Fig. 8 (b). The angle between the centerline of the departure phase and the trace contour is marked as θ_1, which is equal to $\pi/2$-β_s (Fig. 8 (b)). The angle between centerline of slippage phase and trace contour is marked as θ_2. The angle between the centerline of the initial phase and the trace contour is denoted as θ_3. b_1, b_2, and b_3 are the width of the departure phase, slippage phase, and initial phase, respectively. l_1, l_2, and l_3 are the length of the departure phase, the slippage phase, and the initial phase, respectively. The width of the wheel trace imprint b_{all} is the distance of the trace contours and $b_{all}=b_1+b_2+b_3$.

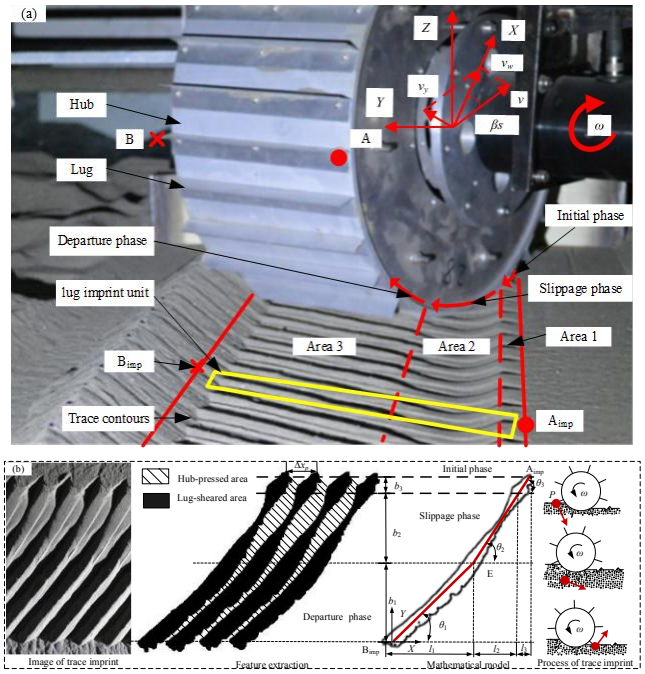

Fig. 8. Photograph and diagram of a wheel trace imprint coupled longitudinal slip and lateral slip: with (a) photograph of wheel trace imprint; and (b) schematic of wheel trace imprint.

B. Lugs Imprint Formation Process

The trace imprint is formed by the lug-soil interaction. The three phases in the process of the lug-soil interaction are as Fig. 8 (b) shows. A_{imp} and B_{imp} are the beginning point and end point in the trace contours separately.

As the lug penetrates into the soil in the initial phase and slippage phase, the edge of lug plows a ditch on the soil with the motion of lug in the initial and slippage phase. It forms the initial lug imprint and the slippage lug imprint. In the departure phase, the lug will dig a pinch of soil. And the process of the departure phase is transient. Accompanied with this process, the trace imprint of the departure phase will be formed. The shape of wheel trace imprint is influenced by the lug shape. For example, if the lug is straight, the shape of wheel trace imprint is a strip groove.

As seen in Fig. 9, A_{imp}, which is in the trace contours, forms at t_{i0} when the lug sticks into the soil. v_p is the resultant velocity of v_w and ωr. The lug leaves the soil at t_{s1}. l_v is the growth vector of the lug imprint caused by v_w from t_{i0} to t_{s1}; $l_{\omega r}$ is the growth vector of the lug imprint caused by ωr from t_{s1} to t_{i0}. l_{vp} is the resultant vector of l_v and $l_{\omega r}$, which is the growth vector of the lug imprint from t_{s1} to t_{i0}. l_{vp} forms the initial and slippage phase of the trace imprint. The centerline of the initial and slippage phase lug imprint is defined as $A_{imp}E$, and the centerline of the departure phase imprint is defined as EB_{imp}.

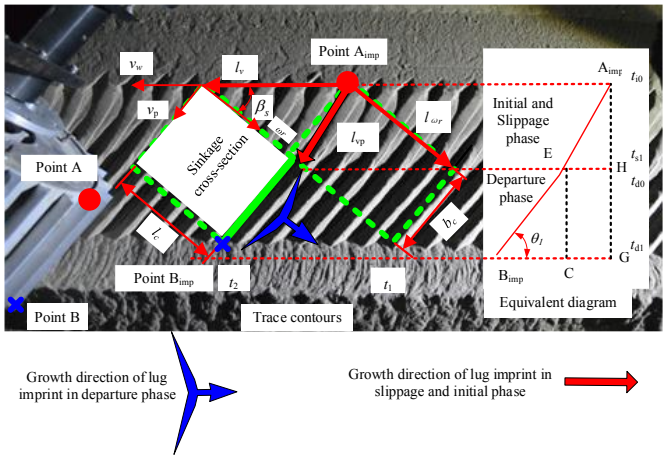

Fig. 9. Photograph of lugs imprint movement on the sinkage cross-section.

C. Kinematics of Lug Trajectory

Figure 10 shows a schematic of wheel motion with coupled longitudinal and lateral slip.

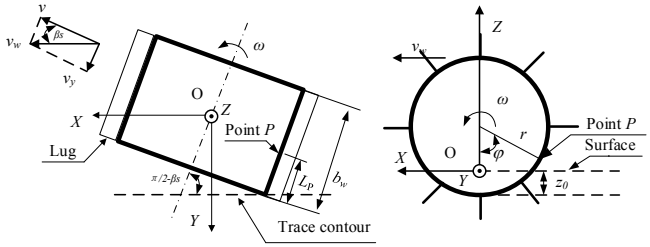

Fig. 10. Schematic of wheel motion with coupled longitudinal and lateral slip, with (a) top view; (b) side view.

The three-dimensional coordinates of point P are (x_p, y_p, z_p). The distance between point P and the side of the wheel is L_P. The trajectory equation of point P is

IEEE Robotics and Automation Letters (RA-L) paper, presented at ICRA 2026, Vienna, Austria. Cite as RA-L paper.

$$\begin{cases} x_p(t)=\int_0^t\left[1-s(\tau)\right]\omega(\tau)r_s\mathrm{d}\tau/\cos\beta_s \\ \quad -\left(r+h_p\right)\sin\left[\int_0^t\omega(\tau)\mathrm{d}\tau\right]\cos\beta_s+\left(b_w/2-L_\mathrm{P}\right)\sin\beta_\mathrm{s} \\ y_p(t)=\left(r+h_p\right)\sin\left[\int_0^t\omega(\tau)\mathrm{d}\tau\right]\sin\beta_s+\left(b_w/2-L_\mathrm{P}\right)\cos\beta_s \\ z_p(t)=\left(r+h_p\right)-\left(r+h_p\right)\cos\left[\int_0^t\omega(\tau)\mathrm{d}\tau\right]-z_0+h_\mathrm{p} \end{cases} \quad (13)$$

The rotation angle of the wheel at time t is defined as $\varphi(t)=\int_0^t\omega(\tau)\mathrm{d}\tau$. Substituting $\varphi(t)$ into (13) yields

$$\begin{cases} x_p(\varphi)=\int_0^\varphi\left[1-s(\psi)\right]r_s\mathrm{d}\psi/\cos\beta_s \\ \quad -\left(r+h_p\right)\sin(\varphi)\cos\beta_s+\left(b_w/2-L_\mathrm{P}\right)\sin\beta_s \\ y_p(\varphi)=\left(r+h_p\right)\sin(\varphi)\sin\beta_s+\left(b_w/2-L_\mathrm{P}\right)\cos\beta_s \\ z_p(\varphi)=\left(r+h_p\right)-\left(r+h_p\right)\cos(\varphi)-z_0-h_p \end{cases} \quad (14)$$

When the wheel rotates, the trajectory of point P is a spiral cycloid under the coupled condition of longitudinal slip and lateral slip. The parameters of the cycloid equation are φ, β_s, r_s, z_0, and $s(\varphi)$. As detailed in the derivation of (10), the width of the trace unit Δx_p can be obtained using (14) as given in (15):

$$\Delta x_\mathrm{p}=\frac{2\pi(1-\bar{s})r_s}{n\cos\beta_s} \quad (15)$$

A trajectory simulation was conducted to show the trajectory of lug in three-dimensional space intuitively, as shown in Fig. 11. Different from simulations with non-lateral slip, the lug reciprocates along Y-axis with wheel rotation because of the side slip angle.

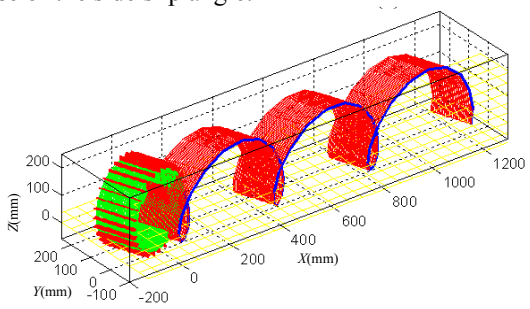

Fig. 11. The simulated wheel lug trajectory.

IV. Estimation Model of Wheel Motion Parameters

A. Wheel Side Slip Angle Estimation Model

As shown in Fig. 9, β_s can be estimated using θ_1 as:

$$\beta_\mathrm{s}=\pi/2-\theta_1 \quad (16)$$

The projection of $A_{imp}E$ perpendicular to v_w is $A_{imp}H = l_c\cos\theta_1$. The projection of $B_{imp}E$ perpendicular to v_w is $HG = b_w\sin\theta_1=b_1$. The length of the departure phase is $B_{imp}C = b_w\cos\theta_1 = l_1$. Therefore, the estimation model of β_s is:

$$\beta_\mathrm{s}=\pi/2-\arctan\frac{b_1}{l_1} \quad (17)$$

B. Wheel Slip Ratio Estimation Model

The wheel slip ratio with side slip angle β_s can be obtained by substituting (16) into (15):

$$\bar{s}=1-\frac{\Delta x_p n\sin\theta_1}{2\pi r_s} \quad (18)$$

Both n and r_s are constant, so $\bar{s}$ can be estimated using θ_1 and Δx_p. Equation (18) can be used to estimate $\bar{s}$ using Δx_p.

C. Estimation Model Verification

To verify these two estimation models, experiments under different side slip angles and slip ratios are performed.

A wheel-soil interaction testbed developed at Harbin Institute of Technology (Fig. 12) was used to control an experimental wheel. v_w was controlled by a drag motor, and ω was controlled by a driving motor. Therefore, the experimental slip ratio can be set.

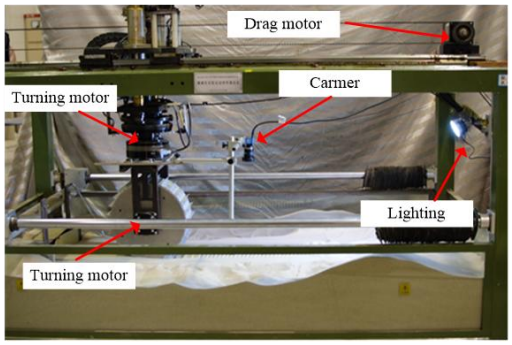

Fig. 12. The vision system of wheel test-bed.

The experiments when the side slip angle is 10°, 20°, 30°, 40° and 50° were conducted, and each condition was carried out three times. v_w was set to 10 mm/s. Both b_1 and l_1 were measured manually to obtain the actual value of β_s, as shown in Fig. 13 (a). The side slip angle estimation model was used to estimate β_s. Comparing with the actual β_s, the relative error and the standard errors are shown in Fig. 13 (b). The relative error can be captured within 3.75%, and the standard error can be captured within 3.0°.

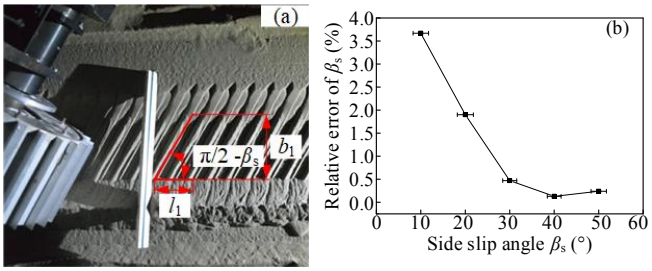

Fig. 13. The β_s measurement method, and experimental verification, with (a) measurement method of β_s, and (b) experimental verification results.

To verify the side slip ratio estimation model when being applied to the condition of β_s = 0°, the experimental $\bar{s}$ =0.1, 0.2, 0.3, 0.4, 0.5, 0.6. The Δx_p were measured manually to estimate slip ratio. Comparing with the experimental set slip ratio, the estimation results are shown in Fig. 14 (a). Comparing with the experimental set slip ratio, the maximum

relative error of the estimated slip ratio can be captured with 10%. When $\bar{s}$ =0.1, the maximum relative error was caused by the estimation error of Δx_p, which can be explained by considering the fact that the height difference between the lug-sheared area and hub-pressed area is too small.

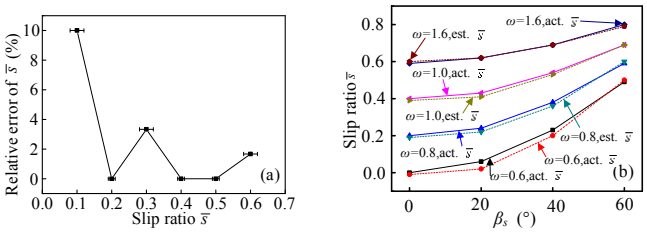

Fig. 14. Experimental results of slip ratio estimation, with (a) relative error of $\bar{s}$ when β_s = 0, and (b) estimation results of $\bar{s}$ with the longitudinal and lateral slip coupled, and wheel angular velocity is in rad/min.

A series of experiments with the coupled longitudinal and lateral slip is also performed to verify the slip ratio estimation model (21). Estimation accuracy of $\bar{s}$ is tested under various values of β_s. Fig. 14 (b) shows the estimation result. The RMS errors of $\bar{s}$ is 0.016, and the RMS errors of $\bar{s}$ are 0.011, 0.024, 0.018, and 0.008, when the side slip angles β_s are 0º, 20º, 40º, and 60º, respectively.

V. Image Processing of Trace Imprint

An image processing method is introduced in Section V to apply this method to the rover missions. The key steps in the image processing, including camera view correction, lighting illumination correction, and trace feature extraction are also described in detail.

A. Image Processing and Trace Feature Extraction

The image processing algorithm processes an original image collected by the vision system, as shown in Fig. 15 (a). The original image needs to be corrected according to the camera transform matrix, and to be intensified by lighting correction of Retinex. To reduce the complexity, the image of the wheel trace imprint was mapped from the RGB to the gray-scale space, and the gray-scale image was then converted into a binary image using the "Otsu" dynamic threshold algorithm, as shown in Fig. 15 (b). The smoothed morphology opening operation image is shown in Fig. 15 (c), and the noise in the binary image may disturb the image feature extraction. Therefore, it was necessary to filter the binary image using small region elimination algorithm.

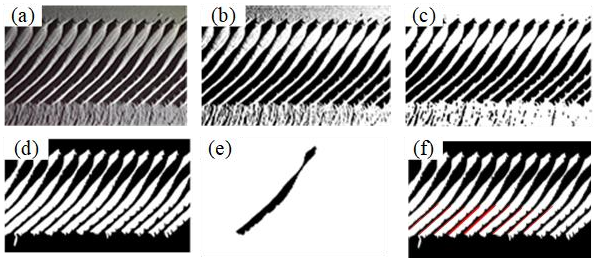

Fig. 15. Image processing results of trace imprint, with (a) original image; (b) binary image; (c) morphology opening operation image; (d) filtered image; (e) segmentation image; (f) extracted trace imprint feature.

The filtered figure retains only the information of the trace imprint, as shown in Fig. 15 (d). Each trace imprint unit was then divided into independent areas using binary segmentation as the precondition of feature extraction process, as shown in Fig. 15 (e). To address the influence of lighting condition, the linear features of the trace imprint were extracted by Hough transformation, as shown in Fig. 15 (f).

The information of the trace imprint can be acquired using the aforementioned feature extraction process, such as the width of trace unit, etc. Then, the wheel motion parameters can be estimated using the trace imprint information and the method proposed in Section IV.

The scale factor is estimated by the actual width and the pixel width of the wheel in the figure. And we assume that the actual width is equal to width of trace imprint when the rover moves along a straight line. This estimation is not rigorous enough because of this assumption.

The wheel trace image processing method to extract trace features for automatic slip state estimation was verified under various lighting conditions. Here, the binary images corrected by Retinex algorithm show distinct trace characteristics regardless of illumination conditions. The experimental results show that the image processing method has a certain adaptability to illumination conditions.

VI. Rover Experimental Verification and Results

A. Experimental Conditions

To validate the proposed method, experiments were also performed using rover testbed which is composed of a rover and a terrain testbed, as shown in Fig. 16.

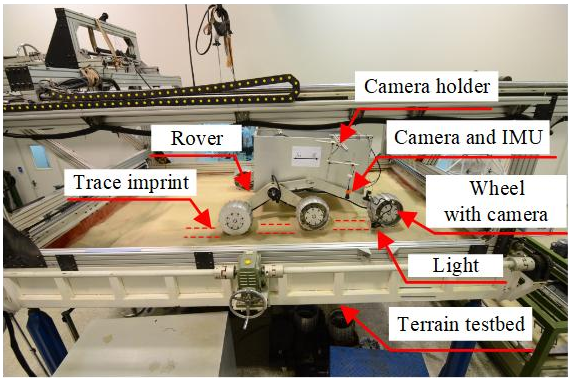

Fig. 16. Photograph of rover experiment on varied terrain.

Terrain testbed can simulate both flat terrain and lateral slope. The rover was equipped with an IMU, a vision collection system, and an image processing system. The vision collection system can collect the digital image of wheel trace imprint and transfer the digital image to image processing system. The image processing system was running on a laptop computer that has a CPU of 2.4 GHz and memory of 1.91 GB, and can extract the features of wheel trace imprint and estimate the side slip angle and slip ratio automatically.

The rover is rocker-bogie configuration with rigid-lugged wheels. The wheel radius is 156 mm; the wheel width is 200 mm. Its wheels can drive independently, so the wheel angular velocity was controlled and collected independently. The wheel forward velocity can be estimated using the rover forward distance and the corresponding consuming time. The actual slip ratio can be calculated using wheel angular velocity and forward velocity.

IEEE Robotics and Automation Letters (RA-L) paper, presented at ICRA 2026, Vienna, Austria. Cite as RA-L paper.

B. Wheel Slip Ratio Estimation

In the experiment, the slip ratio can be changed by the angle velocity differences with measured wheels and other wheels. The velocity of measured wheel is 1 r/min.

The trace imprint features become less obvious with the increase of slip ratio. According to the experimental phenomena, when the wheel slip ratio exceeded 0.6 on sandy terrain, the Δx_p is almost too small to be distinguished, which results in failure of this method. The measured slip ratio in the rover experiments were less than 0.6.

Figure 17 (a) is the trace imprint image of measured wheel when the other wheels velocity is 1 r/min; Fig. 17 (b) is the trace imprint image of measured wheel when the other wheels velocity is 0.8 r/min; Fig. 17 (c) is the trace imprint image of measured wheel when the other wheels velocity is 0.6 r/min; Fig. 17 (d) is the trace imprint image of measured wheel when the other wheels velocity is 0.4 r/min.

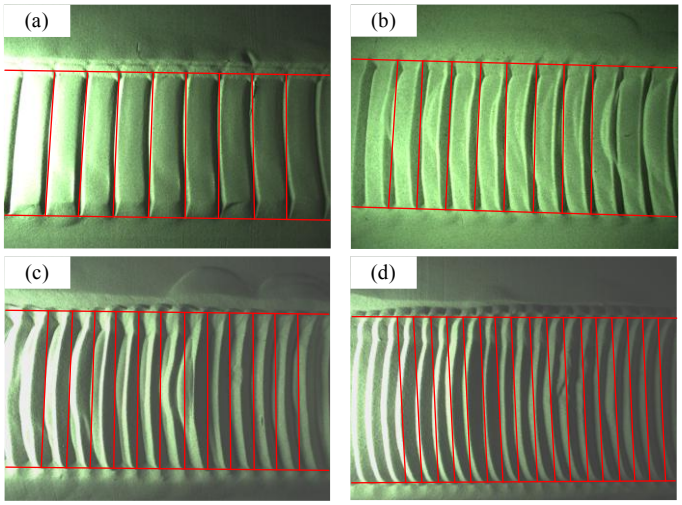

Fig. 17. Wheel trace imprint of various slip ratio, with (a) s=0.03; (b) s=0.13; (c) s=0.34; (d) s=0.55.

Table 1 summarizes the experimental conditions and the estimated s_e in the rover experiment without lateral slip. Comparing with the corresponding measured slip ratio s_m, its absolute error e_a is less than 0.03. The perceived target absolute error of the slip ratio is 0.03 to satisfy requirement of warning rover subsidence and perceiving rover motion state. Under the reported experimental conditions reported in this manuscript, the image processing rate was around 43 Hz. While the visual odometry's frame processing rate was around 13 Hz [8].

Table 1. Wheel slip ratio of rover experiment (e_a=|s_e-s_m|)

ω (r/min)	Δx_p(mm)	s_m	s_e	e_a	v(mm/s)
1	46.0	0.03	0.01	0.02	15.84
0.8	39.1	0.13	0.16	0.03	11.36
0.6	30.7	0.34	0.33	0.01	6.47
0.4	21.5	0.55	0.53	0.02	2.94

In comparison, the maximum absolute error of the estimated rover slip ratio can be captured within 0.15 using motor input torque and encoders, while that can be captured with 0.13 by fusing motor input torque and encoders with VO [18]. Since the rover slip ratio is less than 0.6 to avoid high slip hazard, it can be conducted that the method can works well on both low and moderate slip conditions.

C. Wheel Side Slip Angle Estimation

The accuracy of the proposed method was also verified using lateral slopes experiments. The angular velocity of wheel with camera was 1 r/min, while the angular velocity of other wheels was 0.6 r/min. The rover side slip angle was set as 0°, 5°, 10°, and 20°, as listed in Table 2.

Table 2. Wheel sideslip angle of rover experiment ($e_{\beta s}$=|β_{sr}-β_{se}|)

ω (r/min)	β_{sr} (°)	β_{se} (°)	$e_{\beta s}$ (°)
0.6	0	0.5	0.5
0.6	5	4.3	0.7
0.6	10	10.7	0.7
0.6	20	23.0	3

Figure 18 (a) is the trace imprint image of measured wheel without side slip; Fig.s 18 (b) – (d) show the trace imprint image of measured wheel when the rover run across lateral slopes of 5° angle, 10° angle, and 20° angle, respectively.

Table 2 shows the estimated results of side slip angle in the rover experiment by this method. The absolute error of estimated β_{se} ranges from 0.5° to 3°.

A visual slip angle estimation method was proposed to estimate slip angle using wheel trace, and was named as FTrace [19]. When the ground-truth of slip angle is equal to 5°, the absolute error of the estimated results of FTrace is about 3.12°, while that of our method is 0.7°. Moreover, the ground-truth of slip angle used to validate FTrace ranges from 0° to 12.5°, while that used in this study ranges from 0° to 20°.

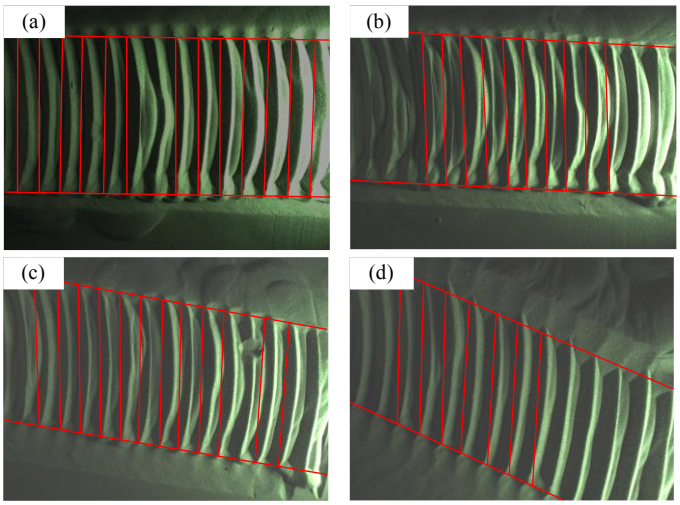

Fig. 18. Wheel trace imprint with various sideslip angle, with (a) β_s =0°; (b) β_s =5°; (c) β_s =10°; (d) β_s =20°.

D. Discussion

The accuracy of the estimation method is greatly affected by the integrity and clarity of the trace imprint pattern. When the wheel trace imprint is badly broken or the lug-sheared area and hub-pressed area are difficult to distinguish, it is hard to work. Sandy terrains are widely distributed on Mars and on the Moon, and even a benign sandy terrain would become an impassable obstacle for planetary rovers. The work relies on the wheel rut pattern, and it works mainly on sandy ground which can maintain relatively distinct (well-patterned) wheel trace imprint. Therefore, this approach is applicable to the vehicles moving with adequate lug imprints, for example, the lunar or Mars rovers moving on deformable terrain but not applicable to crushed stone floors or muddy terrain.

VII. Conclusions and Future Work

This manuscript presented a method for estimating wheel slip ratio and side slip angle by extracting the morphological features of a wheel trace imprint image. The trajectory of lugs was analyzed to reveal the trace formation mechanism and illustrate the effect of the wheel slip and lateral slip angle on the wheel trace imprint. Estimation models of wheel motion parameters have been formulated based on the wheel trace imprint. A trace imprint image processing method based was also present. The proposed method has been verified using a rover test-bed. Comparing with the corresponding measured results, the absolute error of estimated s_e in the rover experiment without lateral slip can be captured within 0.03. Moreover, the absolute error of estimated side slip angle in the rover lateral slopes experiments is less than 3°.

In the future, the reliability of processing images from the field environment, under various conditions of lighting and camera view angle, etc. should be researched further. This method will also be combined with the vision-aided inertial navigation or visual odometry to address overlapping tracks and high-slip conditions. And the influence of lug patters and wheel shapes will be carried out. Improving image processing of wheel trace imprints with higher processing speed and accuracy is another future work. Also, a potential application to motion control of a vehicle will be investigated.

References

[1] L. Ding, H. Gao, Z. Deng, J. Guo, G. Liu, et al., "Longitudinal slip versus skid of planetary rovers' wheels traversing on deformable slopes," *IEEE/RSJ International Conference on Intelligent Robots and Systems*, Tokyo, Japan, 2013, pp. 2842–2848.

[2] M. Maimone, Y. Cheng, and L. Matthies, "Two years of visual odometry on the mars exploration rovers," *Journal of Field Robotics*, vol. 24, no. 3, pp. 169–186, 2007.

[3] L. Ding, R. Zhou, Y. Yuan, H. Yang, J. Li, et al., "A 2-year locomotive exploration and scientific investigation of the lunar farside by the Yutu-2 rover," *Science Robotics*, vol. 62, no. 7, eabj6660, 2022.

[4] K. Yoshida, T. Watanabe, N. Mizuno, and G. Ishigami, "Slip, traction control, and navigation of a lunar rover," *Proc. 6th International Symposium on Artificial Intelligence and Robotics & Automation in Space: i-SAIRAS*, Nara, Japan, 2003, pp. 1-6.

[5] G. Reina, L. Ojeda, A. Milella, J. Borenstein, "Wheel slippage and sinkage detection for planetary rovers", *IEEE/ASME Transactions on Mechatronics*, vol. 11, no. 2, pp. 185–195, 2006.

[6] D. Lhomme-Desages, C. Grand, J.-C. Guinot, F. Ben Amar, "Doppler-based ground speed sensor fusion and slip control for a wheeled rover," *IEEE/ASME Transactions on Mechatronics*, vol. 14, no. 4, pp. 484–492, 2009.

[7] K. Yoshida and H. Hamano, "Motion dynamics of a rover with slip-based traction model," *IEEE International Conference on Robotics & Automation*, Washington, D.C., 2002, pp. 3155–3160.

[8] Nistér D, Naroditsky O, Bergen J. "Visual odometry," *Proceedings of the 2004 IEEE Computer Society Conference on Computer Vision and Pattern Recognition*, Washington, D.C., 2004, pp. 1-8.

[9] C. C. Ward and K. A. Iagnemma, "Dynamic-model-based wheel slip detector for mobile robot on outdoor terrain," *IEEE Transactions on Robotics*, vol. 24, no. 4, pp. 821–831, 2008.

[10] L. Ojeda , D. Cruz , G. Reina, et al, "Current-based slippage detection and odometry correction for mobile robots and planetary rovers," *IEEE Transactions on Robotics*, vol. 22, no. 2, pp. 366-378, 2006.

[11] L. Ding, H. Gao, Z. Deng, K. Yoshida, Y. Nagatani, "Slip ratio for lugged wheel of planetary rover in deformable soil: definition and estimation," *IEEE/RSJ International Conference on Intelligent Robots and Systems*, St. Louis, USA, 2009, pp. 3343-3348.

[12] A. Angelova, L. Matthies, D. Helmick, and P. Perona, "Learning and prediction of slip using visual information," *Journal of Field Robotics*, vol. 24, no. 3, pp. 205–231, 2007.

[13] J. Farrelly and P. Wellstead, "Estimation of vehicle lateral velocity," *IEEE International Conference on Control Applications*, Dearborn, MI, 1996, pp. 552–557.

[14] H. Grip, L. Imsland, T. Johansen, T. Fossen, J. Kalkkuhl, and A. Suissa, "Nonlinear vehicle side-slip estimation with friction adaptation," *Automatica*, vol. 44, no. 3, pp. 611–622. 2008.

[15] D. Bevly, R. Sheridan, and J. Gerdes, "Integrating INS sensors with GPS velocity measurements for continuous estimation of vehicle sideslip and tire cornering stiffness," *American Control Conference.*, Arlington, VA, 2001, pp. 25–30.

[16] A. Milella, G. Reina, and R. Siegwart, "Computer vision methods for improved mobile robot estimation in challenging terrains," *Journal of Multimedia*, vol. 1, no. 7, pp. 49–61, 2006.

[17] G. Reina, G. Ishigami, K. Nagatani, and K. Yoshida, "Vision-based estimation of slip angle for mobile robots and planetary rovers," *IEEE International Conference on Robotics and Automation*, Pasadena, CA, 2008, pp. 486–491.

[18] U. Kono, H. Fujimoto, and Y. Hori, "Localization of wheeled mobile robots from slip ratio estimation with simple model," *IEEE International Conference on Mechatronics*, Kashiwa, Japan, 2021, pp. 1-6.

[19] G. Reina, G. Ishigami, K. Nagatani, "Odometry correction using visual slip angle estimation for planetary exploration rovers,", *Advanced Robotics*, vol 24, no. 30, pp. 359 – 385, 2010.